Molecular-Resolution Imaging of Ionic Liquid/Alkali Halide Interfaces with Varied Surface Charge Densities via Atomic Force Microscopy

Yifan Bao, Yuto Nishiwaki, Touma Kawano, Toru Utsunomiya, Hiroyuki Sugimura, Takashi Ichii*

Department of Materials Science and Engineering, Kyoto University, Yoshida-Honmachi, Sakyo-ku, Kyoto, 606-8501, Japan

*E-mail: ichii.takashi.2m@kyoto-u.ac.jp

Abstract:

Ionic liquids (ILs) in contact with a charged solid surface are known to form layered solvation structures consisting of alternating cation and anion layers. Understanding the response of these layers to surface charge density is vital for IL-based energy storage systems, but it remains inadequately understood. This is partly due to inconsistent experimental conclusions regarding low surface charge density and scarce experimental results for high surface charge density. Here, we probe the solvation structure of ILs on alkali halide surfaces with varied surface orientations: slightly charged RbI(100) and highly charged RbI(111) surfaces to shed light on the above issues, by employing frequency modulation atomic force microscopy (FM-AFM) with a high spatial resolution. Two commonly used ILs, 1-methyl-1-propylpyrrolidinium bis(trifluoromethylsulfonyl)imide ($[C_3mpyr][NTf_2]$) and 1-ethyl-3-methylimidazolium bis(trifluoromethylsulfonyl)imide ($[C_2mim][NTf_2]$) are selected for this study. On the slightly charged RbI(100) surface, we observe alternating cation and anion layers, diverging from the previously proposed monolayer model for IL/alkali halide(100) interfaces. On the highly charged RbI(111) surface, we find crowded layers, which is hardly observed in commonly used ILs due to typically unreachable surface charge densities in electrochemical IL/electrode systems. Our data experimentally elucidates the response of ILs to surface charge density, being expected to deepen our understanding of IL solvation structures on charged solid surfaces. Specifically, observing multilayers on alkali halide(100) surfaces could reconcile some controversial results regarding low surface charge density, whereas detecting crowded layers on alkali halide(111) surfaces offers a new platform for exploring the crowding phenomenon.

KEYWORDS: *liquid/solid interfaces, ionic liquids, solvation structures,*

alkali halide, atomic force microscopy

Introduction

Ionic liquids (ILs) are organic salts with melting points at or near room temperature.[1,2] As advanced solvent-free electrolytes, many of them exhibit beneficial physicochemical properties, such as low vapor pressure, non-flammability, and high electrochemical and thermal stabilities.[1–5] These properties, as well as their unique designability which is tailoring their component to achieve desired characteristics, make ILs attractive for a wide range of applications, such as energy storage, electrodeposition, and electrically controlled lubricantion.[5–7]

Understanding the solvation structure or electric double layer (EDL) at IL/charged solid interfaces is crucial for the applications mentioned above due to its strong correlation with IL-based system performance.[6,8] Since ILs generally comprise ions with large volumes and asymmetrical shapes, the Gouy-Chapmen-Stern model is not directly applicable. For instance, the differential capacitance of IL/electrode interfaces generally displays a bell- or camel-like curve,[9] which deviates from the typical U-shape curve predicted by the Gouy-Chapmen-Stern model and signifies the unique interfacial structure of ILs associated with surface charges.

Experimental approaches with sub-nanometer resolution in the out-of-plane direction, such as X-ray reflectometry (XRR),[10,11] neutron reflectometry (NR),[12] atomic force microscopy (AFM),[13–16] surface force apparatus (SFA),[17] have been utilized to investigate interfacial structures of ILs on charged solid surfaces. It is widely accepted that ILs adopt a layered structure consisting of alternating cation- and anion-rich layers at charged interfaces. Such a structure is considered to originate from *overscreening*;[18] that is, the adsorption layer of counterions overcompensates the surface charge, triggering the formation of an additional co-ion layer over that. This co-ion layer overcompensates again but to a smaller extent, introducing the alternating cation- and anion-rich layers decaying into the bulk within a few nanometers.

3

Nonetheless, there are still several open questions in our comprehension of surface charge density-dependent IL solvation structures over solid surfaces.

Firstly, while theoretical and simulation studies suggest that *overscreening* occurs at low surface charge density close to zero,[18,19] experimental results have not yet reached a consensus. Some studies support the occurrence of *overscreening* at small surface charge densities.[20–22] For instance, Uysal *et al.* observed *overscreening*-induced multilayers at 1-methyl-3-nonylimidazolium bis(trifluoromethylsulfonyl)imide ([C$_9$mim][NTf$_2$])/graphene interfaces using XRR, at the surface charge density as low as approximately 1 μC/cm^2.[21] On the other hand, other studies argue that *overscreening* should occur at larger surface charge densities.[23–26] For instance, using sum frequency generation spectroscopy (SFG), Penalber *et al.* postulate that imidazolium-based ILs form a Helmholtz-like monolayer on NaCl(100) surfaces,[23,24] which exhibit near-zero negative charge densities due to surface relaxation.[27,28] These contradictory results might be attributed to the different ILs and substrates investigated, as well as the difficulty in probing solvation structures at IL/solid interfaces with a high spatial resolution.

Another issue pertains to the interfacial structure of ILs on highly charged surfaces. Kornyshev and coworkers predict the formation of a crowded counterion layer at highly charged interfaces due to the excluded volume between ions (termed crowding).[18,19] That is, the exceptionally high surface charges cannot be screened by a single counterion layer, hence triggering a subsequent counterion layer over that. However, experimental investigation of such a structure is only reported in limited ILs possessing extremely wide electrochemical windows or large ionic sizes.[12,29,30] The reason why crowding is hardly detected in commonly used ILs is partly due to an experimentally unattainable surface charge density that triggers crowding

4

within the electrochemical window for IL/electrode systems, as suggested by simulation studies.[8,31,32]

To shed light on the above issues, we focus on probing solvation structures of ILs on a set of rubidium iodide (RbI) crystal surfaces, as the (100) surface of alkali halide crystals is slightly charged,[24,33] while their (111) face is highly charged.[25] We consider that the IL/alkali halide(100) interfaces reflect the behavior of ILs under low surface charge densities, as weak electrostatic interactions primarily drive the formation of interfacial structures.[23,24,34] Additionally, the motivation is reinforced by the fact that some experimental evidence which support that *overscreening* should occur at larger surface charge densities come from these interfaces.[23,24,34] Consequently, it is considered a thorough examination of these interfaces employing high spatial resolution approaches. On the other hand, the polar (111) surface of alkali halide is expected to facilitate studying the response of ILs to large surface charge densities, because this surface is comprised solely of cations or anions.[25] For comparison, we also introduce an atomically flat mica substrate with a moderate surface charge density,[35] which is higher than RbI(100) but lower than RbI(111). Through this methodology, we anticipate capturing the characteristics of solvation structures at IL/solid interfaces regarding low, moderate, and high surface charge densities.

In this study, frequency modulation (FM-) AFM with a high spatial resolution is employed to investigate the solvation structures of ILs on RbI(100), mica and RbI(111) surfaces.[36,37] Two commonly used ILs, 1-methyl-1-propylpyrrolidinium bis(trifluoromethylsulfonyl)imide ([C_3mpyr][NTf$_2$]) and 1-ethyl-3-methylimidazolium bis(trifluoromethylsulfonyl)imide ([C_2mim][NTf$_2$]) are studied, allowing us to propose similar underlying mechanisms. By means of high-resolution topographic imaging, we first characterize the atomic flatness and

5

cleanness of both RbI(100) and (111) surfaces in both ILs. This serves as prerequisite for credible investigation of solvation structures over the solid substrate surfaces. By means of two-dimensional (2D) frequency shift (Δf) mapping, we then demonstrate the existence of alternating cation and anion layers on slightly charged RbI(100) surfaces and solvation structures originating from *crowding* on highly charged RbI(111) surfaces.

Results and Discussion

Structural Characterization of the RbI (111) and (100) Surfaces in ILs

RbI crystals with exposed (111) surfaces were prepared using epitaxial growth on a mica substrate from IL solutions (refer to Experimental Section for more details). This method produced RbI crystals immersed in ILs, as shown in Figures 1b and c. The structure of the crystals was characterized by optical microscopy (OM), X-ray diffraction (XRD), and in situ FM-AFM. Figure 1c presents a typical OM image of RbI crystals in [C_3mpyr][NTf_2] solutions, showing plate-like morphologies with triangular bases, as marked by red circles. It can also be seen that a very small number of crystals exhibit rectangle bases, marked by purple rectangles. Triangular-based RbI crystals indicate that the RbI[111] axis is perpendicular to the mica substrate,[38] and agree with epitaxial growth of RbI crystals on mica substrates from aqueous solutions.[38] However, crystals grown from aqueous solutions formed pyramids with exposed {100} facets,[38] which is different from the plate-like crystals in our study. Crystal orientation was further analyzed using XRD. Figure 1d shows the XRD pattern of RbI crystals grown on a mica substrate. The detected peaks correspond to RbI{111} and (100) planes, along with the mica substrate. Notably, the intensities of the peaks from RbI{111} planes were approximately 1000 times greater than those from RbI(100) planes, confirming the predominant growth of (111)-oriented RbI crystals. Considering that (111)-oriented RbI crystals possibly expose {100} planes on their surfaces, as seen in crystals grown from aqueous solutions,[38] we employed in

6

situ FM-AFM to examine the surface structure of RbI crystals grown on a mica substrate. Figures 2a and b show the obtained AFM topographic images in [C$_3$mpyr][NTf$_2$] and [C$_2$mim][NTf$_2$]. Height profiles along lines A-B and C-D (Figures 2e,f) demonstrate that step heights are always close to single or multiple integers of 0.42 nm, which is in agreement with twice the interplanar spacing along the RbI[111] axis (Figure 1a). These findings imply that atomic steps are kept in ILs and only one type of ion, either Rb$^+$ or I$^-$, is exposed. This indication is further supported by in situ imaging of the crystal growth of RbI(111), at which the stepwise surface position shifts of ca. 0.42 nm were observed (Figure S1 and its corresponding text in the Supporting Information). The termination plane of RbI crystals in contact with negatively charged mica substrates was previously proposed to consist of Rb$^+$ ions,[39] which has been recently confirmed by XRR and MD simulations.[40] Therefore, based on electrostatic considerations, the termination plane in contact with ILs is most likely an iodine layer.
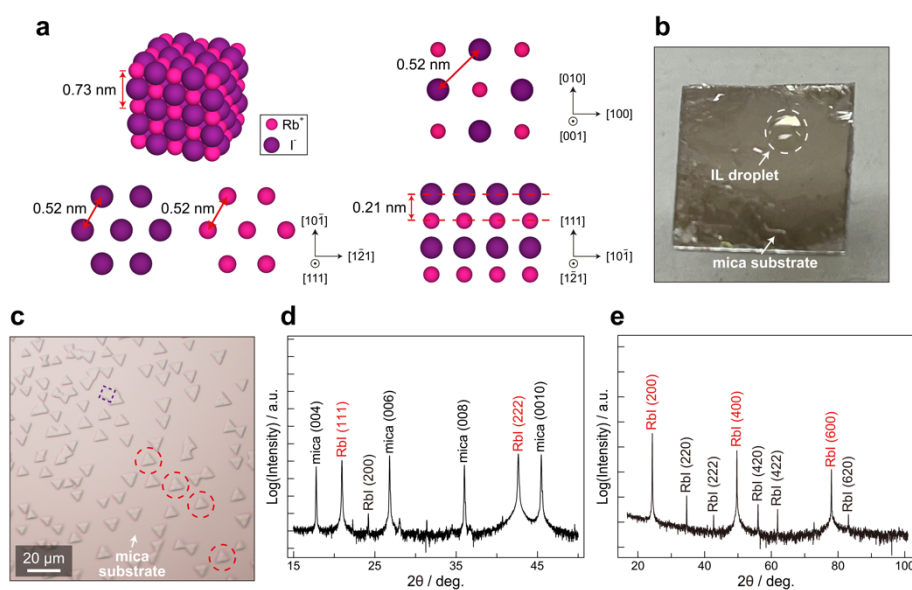

Figure 1. (a) Atomistic model of an RbI crystal, including its (100) and (111) surfaces. (b) Digital photograph of an RbI crystal sample with a droplet of RbI-dissolved [C$_3$mpyr][NTf$_2$] solution on a mica substrate. (c) Optical microscopy image of RbI crystals grown on a mica substrate from an RbI-dissolved [C$_3$mpyr][NTf$_2$] solution. Typical triangular-based RbI crystals are marked with red broken circles. A RbI crystal with a rectangular base is marked with a purple broken rectangle. (d) XRD pattern of RbI crystals grown on a mica substrate. (e) XRD pattern of RbI crystals obtained through evaporation crystallization.
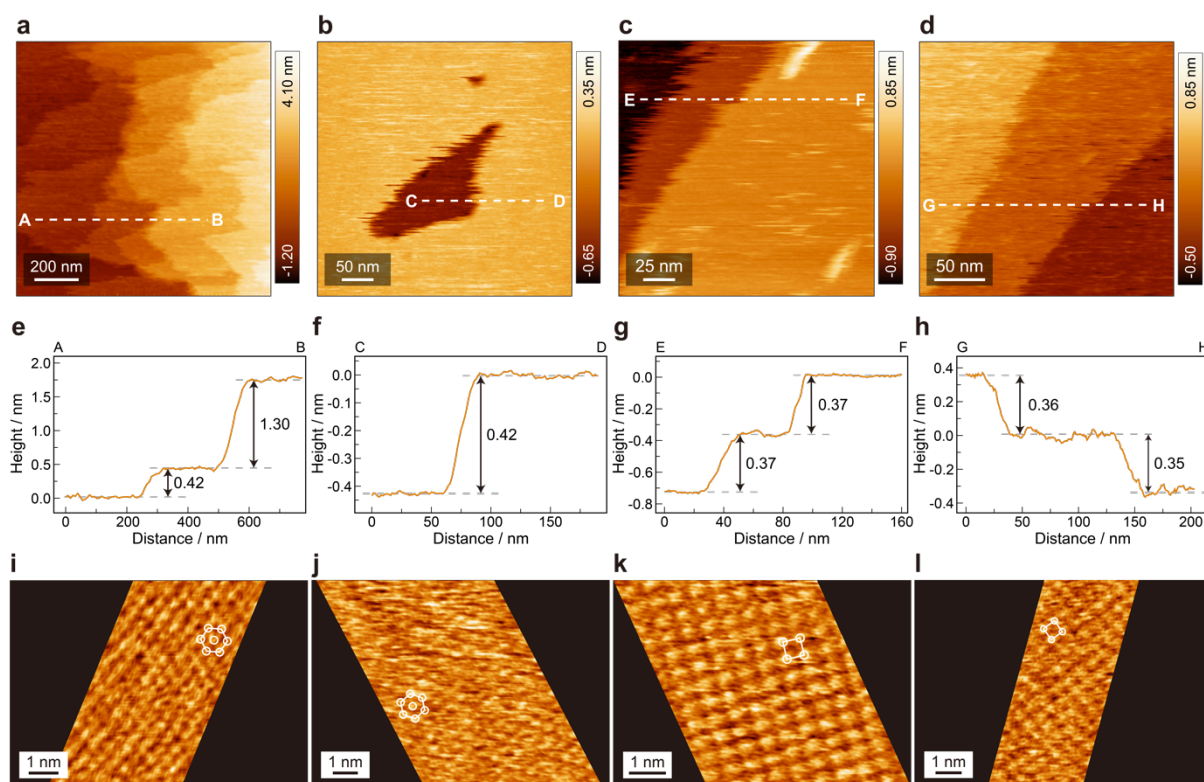
7

Figure 2. Large-scale topographic images obtained for: (a) [C$_3$mpyr][NTf$_2$]/RbI(111) (Frequency shift Δf = 10 Hz, Oscillation amplitude $A_{\text{p-p}}$ = 292 pm), (b) [C$_2$mim][NTf$_2$]/RbI(111) (Δf = 11 Hz, $A_{\text{p-p}}$ = 198 pm), (c) [C$_3$mpyr][NTf$_2$]/RbI(100) (Δf = 10 Hz, $A_{\text{p-p}}$ = 194 pm), (d) [C$_2$mim][NTf$_2$]/RbI(100) (Δf = 4.5 Hz, $A_{\text{p-p}}$ = 198 pm). Cross-sectional height profiles measured along: (e) line A-B, (f) line C-D, (g) line E-F, (h) line G-H. Atomic-scale topographic images obtained for: (i) [C$_3$mpyr][NTf$_2$]/RbI(111) (Δf = 13 Hz, $A_{\text{p-p}}$ = 231 pm), (j) [C$_2$mim][NTf$_2$]/RbI(111) (Δf = 13 Hz, $A_{\text{p-p}}$ = 198 pm), (k) [C$_3$mpyr][NTf$_2$]/RbI(100) (Δf = 10 Hz, $A_{\text{p-p}}$ = 194 pm), (l) [C$_2$mim][NTf$_2$]/RbI(100) (Δf = 20 Hz, $A_{\text{p-p}}$ = 191 pm).

The RbI crystal surfaces in both ILs were further resolved at the atomic scale. Figures 2i,j show hexagonally arranged bright spots, spaced around 0.52 nm apart, matching the distance between adjacent I$^-$ ions on the RbI(111) plane (Figure 1a). At this point, it is unclear whether the images present the bare RbI(111) surface or a tightly adsorbed cation layer impenetrable by the AFM tip because [C$_3$mpyr]$^+$ and [C$_2$mim]$^+$ cations are similar in size to the interatomic distances of the RbI(111) planes (Figure 3b and its corresponding captions). A previous STM study suggested that [C$_4$mpyr]$^+$ cations adsorbed onto Au(111) surfaces could form compact arrays with spacings close to 0.5 nm when only their rings are directly bound to the substrate.[41]

8

For convenience, we refer to the obtained surface as "apparent surface". Nevertheless, the observed interatomic distance (~0.52 nm) and hexagonal symmetry in Figures 2i and 2j align with the bulk truncated RbI(111) plane, strongly implying that the RbI(111) surfaces did not undergo apparent reconstruction in ILs. Furthermore, the successful high-resolution imaging confirms that the RbI(111) surfaces are atomically clean and flat, ensuring that the solvation structures are formed at IL/RbI(111) interfaces directly.[42–45]

RbI crystals with (100) surfaces were prepared by evaporation crystallization from aqueous solutions with subsequent cleavage (see Experimental Section for more details). The XRD pattern (Figure 1e) reveals the intensities of the peaks from {100} planes to be approximately 1000 times greater than those from other planes, confirming the preferential (100) orientation of the crystals. The surface structure of the prepared crystals was further characterized using FM-AFM in ILs. Figures 2c,d show typical large-scale topographic images of the crystal surfaces in [C_3mpyr][NTf$_2$] and [C_2mim][NTf$_2$]. Both surfaces show step-terrace structures with step heights of about 0.37 nm, as indicated by height profiles E-F (Figure 2g) and G-H (Figure 2h). This value is in good agreement with the interplanar spacing normal to the RbI(100) surface, which is half of the lattice constant of RbI (Figure 1a). Atomic-resolution imaging in both ILs was achieved as well, as shown in Figures 2k,l. The observed square lattice has a period of about 0.52 nm, consistent with the expected spacing between the nearest like-charged ions on the RbI(100) plane. It is most likely that the bare RbI(100) surfaces were detected in both ILs, which will be discussed later. This result aligns with previous FM-AFM studies on alkali halide surfaces in UHV, aqueous solution, and ILs,[25,46–49] which indicate that either cations or anions are observed on the surface. Our findings confirm that the RbI(100) surfaces remain stable after immersion in ILs, with their atomic-level cleanness and flatness.

9

Characterizing the Solvation Structure at IL/Mica Interfaces

Firstly, we investigated the solvation structure of two ILs, [C$_3$mpyr][NTf$_2$] and [C$_2$mim][NTf$_2$], on moderately charged mica surfaces. Previous studies reported that mica typically exhibits a surface charge density of approximately 20 μC/cm^2 when immersed in ILs.[35] This served as a basis for subsequent comparison and explanation of solvation structures observed on the slightly charged RbI(100) and highly charged RbI(111) surfaces. As depicted in Figure 3, two-dimensional (2D) frequency shift (Δf) mapping was used to obtain molecular-resolution cross-sectional views of the solvation structure at IL/solid interfaces. Figures 4a,b show representative 2D Δf maps obtained in [C$_3$mpyr][NTf$_2$] and [C$_2$mim][NTf$_2$]. A continuous stripe-like contrast along the apparent surfaces (grey-colored) signifies uniform solvation layers at both IL/mica interfaces. The apparent surface observed in [C$_3$mpyr][NTf$_2$] is slightly curved, which is ascribed to a nonlinear thermal drift in the z direction during scanning.
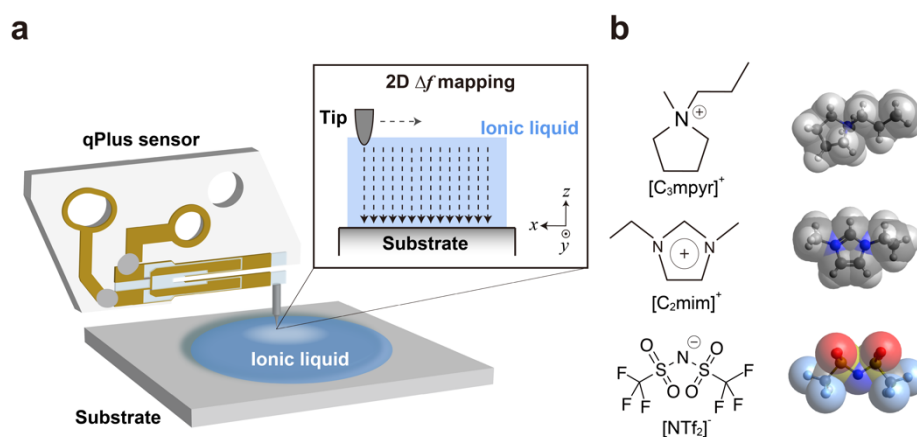

Figure 3. (a) A schematic of AFM imaging in liquid using a qPlus sensor. Inset: A schematic of 2D Δf mapping measurements at a liquid/solid interface. (b) Molecular structure of ILs used in this study. The dimensions of [C$_3$mpyr]$^+$, [C$_2$mim]$^+$ and [NTf$_2$]$^-$ are reported to be $0.8 \times 0.5 \times 0.6$ nm^3, $0.85 \times 0.55 \times 0.28$ nm^3, and $1.09 \times 0.51 \times 0.47$ nm^3, respectively.[17,50–52] Their outer van der Waals surfaces with internal ball and stick structures are presented (C: gray; H: white; N: blue; O: red; S: yellow; F: light blue).
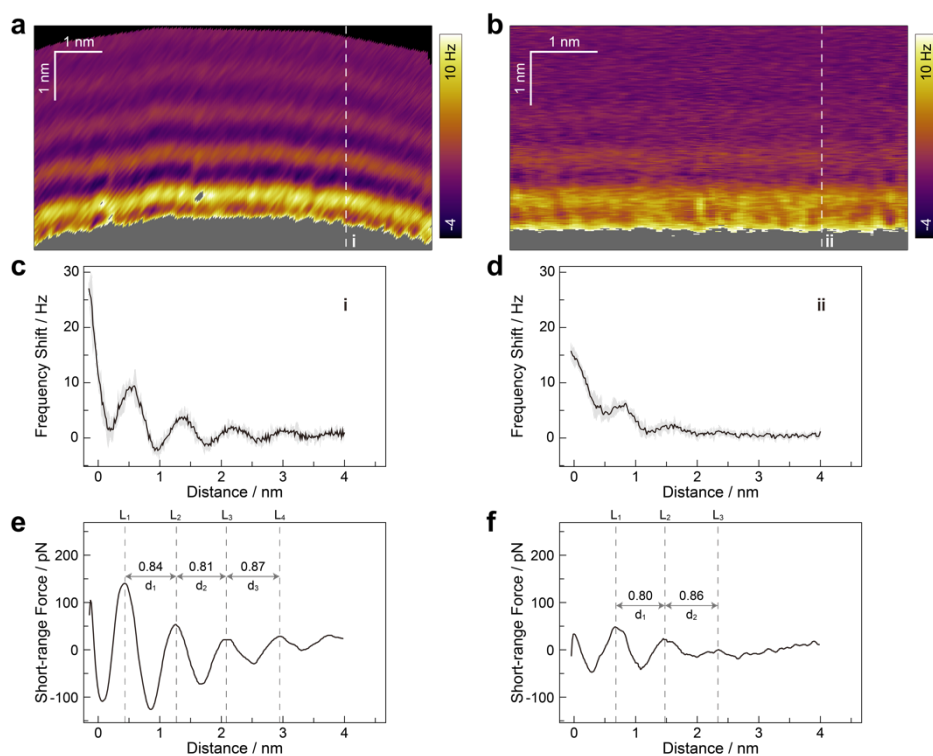
Figure 4. 2D Δf maps obtained for: (a) [C$_3$mpyr][NTf$_2$]/mica ($A_{\text{p-p}}$ = 194 pm), and (b) [C$_2$mim][NTf$_2$]/mica interfaces ($A_{\text{p-p}}$ = 186 pm). (c-d) Δf versus distance profiles along line i and line ii, respectively. The black line represents the averaged profile. The grey area shows the corresponding two standard deviation. Distance is measured as a relative value from the initial set point. (e-f) Short-range force versus distance profiles corresponding to c and d, respectively.

To quantitatively analyze solvation structures, we extracted Δf versus tip-to-sample distance profiles from the maps and converted them into short-range force versus tip-to-sample distance profiles (henceforth referred to as Δf and short-range force profiles). Before conversion, Δf profiles were averaged with adjacent 10 profiles to improve the signal-to-noise ratio.[53] The averaged Δf profiles in [C$_3$mpyr][NTf$_2$] and [C$_2$mim][NTf$_2$] are presented in Figures 4c and d, respectively. As the tip-to-sample distance decreases, both Δf profiles exhibit significant oscillatory behavior due to the presence of solvation layers, followed by a monotonic increase upon direct interaction between the tip and the apparent surface. We then converted these Δf

11

profiles to force profiles using the formula proposed by Sader and Jarvis,[54] as shown in Figure S2. The profiles consist of a long-range background with superimposed oscillatory short-range components. Focusing on the short-range solvation forces, we subtracted the background force from the original profiles to obtain the short-range force profiles. A double-exponential function was used to fit the force profiles. A similar fitting procedure has also been employed in recent AFM studies.[43,45]

The short-range force profiles at both IL/mica interfaces (Figures 4e,f) exhibit oscillatory behavior featuring several peaks. We designate the peak closest to the surface as L_1 and label subsequent peaks with incremental higher indices. Peak separations, which are the distance between maximum points of neighboring peaks, are summarized in Table 1. Additionally, the intensities of solvation force peaks are plotted in Figure 8 and Table S1. Here, a solvation force peak was measured from each local maximum to the next minimum over extended distances. This approach parallels the analysis of FM-AFM force profiles at aqueous solution/solid and IL/solid interfaces, as conducted by Kilpatrick et $al.$,[55] Utsunomiya et $al.$,[56] and Umeda et $al.$[15,57] Concerning peak separation, $[C_3mpyr][NTf_2]$ showed four peaks approximately 0.84 nm apart, whereas $[C_2mim][NTf_2]$ had three peaks roughly 0.78 nm apart. Both peak separations are consistent with the ion pair diameters of the respective ILs, that is about 0.80 nm for $[C_3mpyr][NTf_2]$ and about 0.75 nm for $[C_2mim][NTf_2]$. These ion pair diameters were calculated from densities assuming a cubic packing geometry, based on the method proposed by Horn et $al.$[58] When concerning solvation force peak intensity, it is clear to see that those in $[C_3mpyr][NTf_2]$ are higher than those in $[C_2mim][NTf_2]$.

Table 1. Peak separations extracted from the short-range force profiles of IL/mica interfaces

	d_1 (nm)	d_2 (nm)	d_3 (nm)
[C$_3$mpyr][NTf$_2$]	0.85 ± 0.03	0.84 ± 0.04	0.83 ± 0.07
[C$_2$mim][NTf$_2$]	0.79 ± 0.05	0.76 ± 0.07	—

The interval indicates the standard deviations from 10 data sets collected using the same tip in [C$_3$mpyr][NTf$_2$] and 6 data sets collected using the same tip in [C$_2$mim][NTf$_2$]

Establishing a quantitative correlation between the dynamic AFM force profile and molecular density distribution in ILs is still ongoing. The widely used solvent tip approximation is only validated for water molecules in dilute electrolytes.[59–61] Nevertheless, Amano and coworkers have qualitatively explored the relationship between detected forces and IL ion density distributions.[62] Their model directly correlates the force profile obtained by a charged tip with the density distribution of like-charged species in ILs. That is, the solvation force is positively correlated to the deviation of the density distribution of like-charged species.[62] In this study, we employed tungsten tips, which likely bear a negative charge due to an oxide layer. Then, the tip apex is likely to be solvated by cations in ILs. Consequently, the oscillatory behavior in the force profiles (Figures 4e,f) indicates the detection of cationic or anionic layers with a thickness comparable to the ion pair diameter of the respective ILs. Numerous studies on IL/charged solid interfaces, employing XRR,[10,11] AFM,[15,63] and simulations,[11] have reported layered structures with thickness matching the ion pair size, implying alternating cation and anion layers.

Characterizing the Solvation Structure at IL/RbI(100) Interfaces

To explore the response of IL solvation structures to low surface charge density, we visualized [C$_3$mpyr][NTf$_2$]/RbI(100) and [C$_2$mim][NTf$_2$]/RbI(100) interfaces with a nearly-zero surface charge (see Experimental Section). The 2D Δf maps (Figures 5a,b) reveal stripe-

13

like contrasts in both ILs. It is noted that the strip-like contrast at the $[C_2mim][NTf_2]/RbI(100)$ interface is notably weaker (indicated with grey open arrows) than that at the $[C_3mpyr][NTf_2]/RbI(100)$ interface. The averaged Δf profile of the $[C_2mim][NTf_2]/RbI(100)$ interface (Figure 5d) shows oscillations, evidencing the existence of solvation layers. We converted the Δf profiles at both interfaces (Figures 5c,d) into short-range force profiles (Figures 5e,f). Peak separations and intensities of solvation force peaks are summarized in Table 2 and Figure 8, respectively. For $[C_3mpyr][NTf_2]/RbI(100)$, three peaks ($L_1$-$L_3$) were identified with an interpeak distance of around 0.83 nm. For $[C_2mim][NTf_2]/RbI(100)$, the interpeak distance from L_1 to L_2 was approximately 0.66 nm. The peak for L_1 exhibited a similar intensity to that for L_2. Compared to those on mica, short-range force profiles on RbI(100) surfaces are characterized by two analogous features: first, peak separations are comparable to the ion pair diameter of the respective ILs, indicating alternating cation and anion layers; second, $[C_3mpyr][NTf_2]$ presents a more pronounced solvation structure than $[C_2mim][NTf_2]$, with more layers and stronger forces. The influence of different surface charge densities on solvation structures will be discussed later.
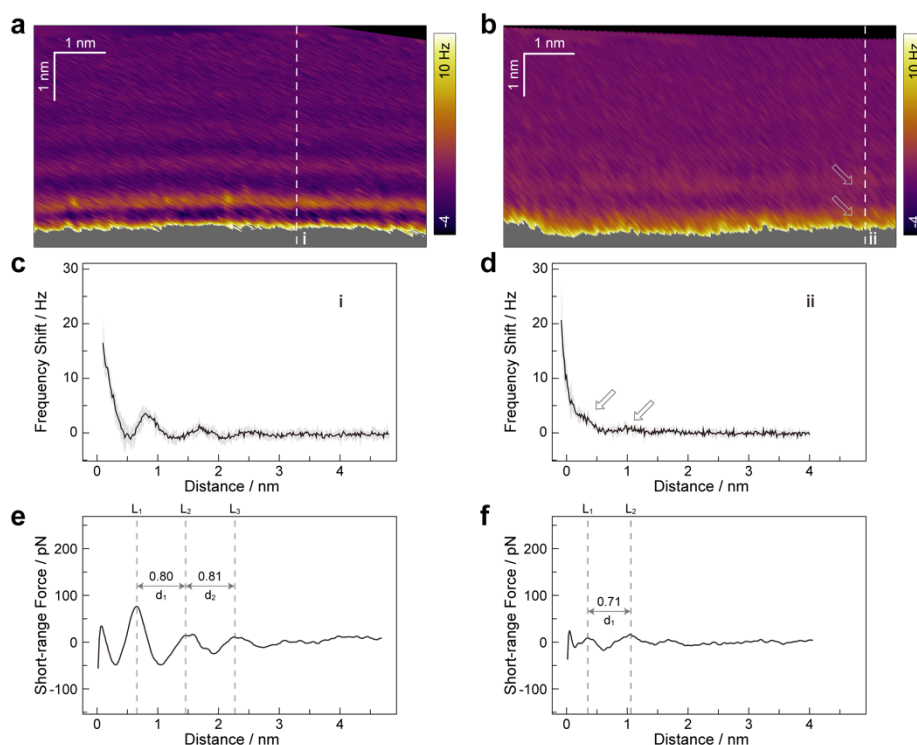
Figure 5. 2D Δf maps obtained for: (a) [C$_3$mpyr][NTf$_2$]/RbI(100) ($A_{p\text{-}p}$ = 189 pm), and (b) [C$_2$mim][NTf$_2$]/RbI(100) interfaces ($A_{p\text{-}p}$ = 191 pm). (c-d) Δf versus distance profiles along line i and line ii, respectively. The black line represents the averaged profile, with the grey area showing the corresponding two standard deviation. Distance is measured as a relative value from the initial set point. (e-f) Short-range force versus distance profiles corresponding to c and d, respectively. Grey open arrows in (b) and (d) indicate the weak oscillations detected at [C$_2$mim][NTf$_2$]/RbI(100) interfaces.

Table 2. Peak separations extracted from the short-range force profiles of IL/RbI(100) interfaces

	d_1 (nm)	d_2 (nm)	d_3 (nm)
[C$_3$mpyr][NTf$_2$]	0.84 ± 0.05	0.83 ± 0.08	—
[C$_2$mim][NTf$_2$]	0.66 ± 0.06	—	—

The interval indicates the standard deviations from 8 data sets collected using the same tip in [C$_3$mpyr][NTf$_2$] and 6 data sets collected using the same tip in [C$_2$mim][NTf$_2$].

We next determined the origin of the apparent surface at the IL/RbI(100) interfaces. High-resolution topographic images (Figures 2k,l) reveal similar square lattices with a spacing of

~0.52 nm in both ILs, consistent with the interatomic distance of like-charged ions on RbI(100) surfaces (Figure 1a). As with the cases of RbI(111), the comparable dimensions of $[C_3mpyr]^+$ and $[C_2mim]^+$ cations make it hard to exclude the possibility that the observed square lattices indeed represent adsorbed cations. To address this, we observed the apparent surfaces at IL/NaCl(100) interfaces based on the following ideas: (i) Similar solvation structures are expected to form on NaCl(100) and RbI(100) surfaces due to their similar ionic nature and surface charge densities (see Figures S3 and S4); (ii) The spacing between like-charged ions on NaCl(100) plane (0.397 nm) is too small to accommodate a single $[C_3mpyr]^+$ or $[C_2mim]^+$ cation. Figures S3 and S4 present high-resolution topographic images on NaCl(100) surfaces in $[C_3mpyr][NTf_2]$ and $[C_2mim][NTf_2]$. Similar square lattices with a spacing of about 0.40 nm are obtained. This value agrees with the distance between like-charged ions on NaCl(100) and is smaller than the sizes of individual $[C_3mpyr]^+$ or $[C_2mim]^+$ cations, indicating that the bare NaCl(100) surface was most likely visualized in both ILs. It is noted that NaCl(100) surface likely has a higher surface charge density than RbI(100) due to more pronounced surface rumpling.[64] Then, a weaker electrostatic attraction between cations and the RbI(100) surface can be inferred. These results suggest that the apparent surfaces approached at the $[C_3mpyr][NTf_2]$/RbI(100) and $[C_2mim][NTf_2]$/RbI(100) interfaces are likely bare RbI(100) surfaces, rather than adsorption layers. Combined with the analysis of solvation structures mentioned above, we addressed the interfacial structure of $[C_3mpyr][NTf_2]$ and $[C_2mim][NTf_2]$ on the weakly charged RbI(100) surfaces. This structure consists of alternating cation and anion layers, and the innermost layer interacts so weakly with the surface that the AFM tip can penetrate them.

However, earlier FM-AFM studies did not detect layered solvation structures at 1-butyl-1-methylpyrrolidinium tris(pentafluoroethyl)trifluorophosphate ($[C_4mpyr][FAP]$)/KCl(100),[48] and 1-butyl-3-methylimidazolium hexafluorophosphate ($[C_4mim][PF_6]$)/KBr(100) interfaces.[25]

In the former case, the discrepancy may stem from disruption of the solvation structure due to an unstable substrate. This is supported by the visualization of layered structures induced by substrate dissolution in the 2D Δf map.[48] Conversely, the RbI(100) and NaCl(100) surfaces were stable during observation, and we did not obtain substrate dissolution-induced layers. This emphasizes the imperative of carefully considering substrate stability for studying solvation structures at IL/alkali halide interfaces. Regarding the [C$_4$mim][PF$_6$]/KBr(100) interface, the discrepancy may be attributed to the large amplitude applied ($A_{\text{p-p}}$ is about 700 pm), resulting in less sensitivity to short-range solvation forces. Considering the observed weak solvation structures in [C$_2$mim][Tf$_2$N] on RbI(100) and NaCl(100) within this study, we deem this assumption to be reasonable.

Characterizing the solvation structure at IL/RbI(111) interfaces

We next investigated how the interfacial solvation structure of ILs responds to high surface charge density by probing IL/RbI(111) interfaces, estimated to have a surface charge density of about 35 μC/cm^2 (see Experimental Section). Figures 6a and b display the 2D Δf maps acquired on RbI(111) surfaces in [C$_3$mpyr][NTf$_2$] and [C$_2$mim][NTf$_2$], respectively. Stripe-like contrasts along the interfaces are a clear indication of ordered solvation layers. We observed a consistent positive shift of ~0.4 nm in the z direction during 2D Δf mapping in [C$_3$mpyr][NTf$_2$], as indicated by the white arrow in Figure 6a. Considering that the map was obtained in a region showing crystal surface growth (as seen in topographic imaging) and the position shifts of trigger Δf agree with the twice interplanar spacing along the RbI(111) axis (refer to Figure S1 and the corresponding text in the supporting information), we ascribe these positive position shifts to the growth of RbI(111) surface. This furnishes robust evidence that the detected solvation structures are indeed located above the highly charged RbI(111) surface.
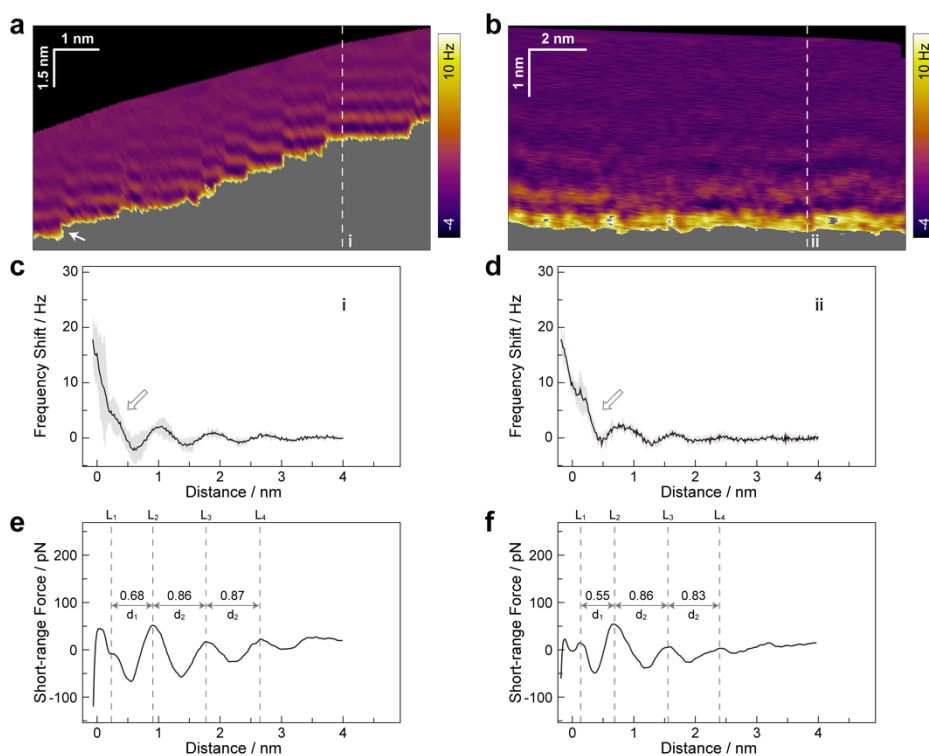
17

Figure 6. 2D Δf maps obtained for: (a) [C$_3$mpyr][NTf$_2$]/RbI(111) ($A_{\text{p-p}}$ = 231 pm), and (b) [C$_2$mim][NTf$_2$]/RbI(111) interfaces ($A_{\text{p-p}}$ = 198 pm). (c-d) Δf versus distance profiles along lines i and ii, respectively. The black line represents the averaged profile, with the grey area showing the corresponding two standard deviation. Distance is measured as a relative value from the initial set point. (e-f) Short-range force versus distance profiles corresponding to c and d, respectively. A white arrow in (a) indicates a typical step originating from the growth of RbI(111) surfaces during imaging. Grey open arrows in (e) and (f) highlight shoulder-like innermost peaks observed at both interfaces.

Interestingly, typical Δf profiles of [C$_3$mpyr][NTf$_2$] and [C$_2$mim][NTf$_2$] (Figures 6c,d) feature a distinctive innermost peak with a shoulder-like appearance (indicated by grey open arrows), absent on moderately charged mica surfaces. For [C$_2$mim][NTf$_2$], some profiles without shoulder-like innermost peak, were also found occasionally (Figure S5). We converted the Δf profiles (Figures 6c,d) into corresponding short-range force profiles, and peak separations and intensities of solvation force peaks were summarized in Table 3 and Figure 8, respectively. The short-range force profiles on RbI(111) (Figures 6e,f) show two primary

features. First, d_1 for both ILs is smaller than their respective ion pair diameters. For [C$_3$mpyr][Tf$_2$N] (Table 3), d_1 shows 70% of other external peak separations. Similarly, for [C$_2$mim][Tf$_2$N] (Table 3), d_1 is around 60% of other external peak separations. Second, while the intensity of solvation force peaks for L$_2$-L$_4$ are attenuated from the surface as seen with mica and RbI(100) in this study and previous results,[15,62,63,65] L$_1$ displays a reduced intensity compared to L$_2$ (see Figure 8). Such a phenomenon, to the best of our knowledge, has not been reported previously. However, the qualitatively similar changes in solvation structure across different ILs do suggest a common underlying mechanism at the internal layer structure.

Table 3. Peak separations extracted from the short-range force profiles of IL/RbI(111) interfaces

	d_1 (nm)	d_2 (nm)	d_3 (nm)
[C$_3$mpyr][NTf$_2$]	0.63 ± 0.05	0.86 ± 0.02	0.88 ± 0.02
[C$_2$mim][NTf$_2$]	0.49 ± 0.06	0.81 ± 0.06	0.81 ± 0.03

The interval indicates the standard deviations from 7 data sets collected using the same tip in [C$_3$mpyr][NTf$_2$] and 9 data sets collected using the same tip in [C$_2$mim][NTf$_2$].

To elucidate the origin of this solvation structure, we first checked whether it exists in a liquid state. Figures S6a and b display the 2D energy dissipation maps obtained simultaneously with the 2D Δf maps in Figures 6a,b. The excitation voltage (V_{exc}) for keeping oscillation amplitude shows a linear relationship with energy dissipation. A monotonic increase in V_{exc} as the tip-sample distance decreases (see Figures S6c and d) indicates a similar increase in energy dissipation. Previous studies using FM-AFM have shown that a monotonic increase in energy dissipation as the tip approaches the surface indicates the liquid-like behavior of the detected interfacial structure; otherwise, some oscillations should be present.[66,67] As a result, we can conclude that the detected solvation structure at IL/RbI(111) interfaces exists in a liquid-like state, not in a solid-like state.

Considering the presence of four ion types at the IL/RbI(111) interfaces, IL cations and anions, along with dissolved Rb^+ and I^- ions, the interfacial structure is expected to be complex. However, d_1 varies in different ILs (0.63 nm in $[C_3mpyr][Tf_2N]$ and 0.49 nm in $[C_2mim][Tf_2N]$), and d_1 is notably larger than the dimensions corresponding to metal ions and anions. For instance, AFM identified an innermost layer with a spacing of ~0.3 nm at the $[C_4mpyr][Tf_2N]$/Au(111) interface in the presence of Li^+ ions, and this observation was attributed to the interaction between $[Tf_2N]^-$ anions and Li^+ ions adsorbed onto the substrate.[68] Consequently, we consider that L_1, along with external peaks (L_2, L_3, etc.), most likely reflects the molecular layering of IL ions.

Based on previously reported solvation structure models, we present the plausible ones in Figures 7a and b. Both models feature a distinct "thicker" counterion layer composed of two cation sublayers. This is consistent with the expected *crowding* of counterions in high surface charge density environments.[18] The primary difference between the two models is their explanation for the smaller d_1 in the force profiles, attributed to ion layers within the solvation structure. In Figure 7a, as the AFM tip approached the surface, it encountered a strongly bound cation layer that appeared to be the apparent surface. The d_1 represents the spacing between the second and third cation layers, corresponding to the outer sublayers of the crowded layer and the external cation layer, respectively. The reduced d_1 compared to external peak separations, which are comparable to the ion pair diameter of respective ILs, is likely due to cations in the second layer tilting or aligning parallel to the surface through electrostatic interaction. In Figure 7b, the bare RbI(111) surface is identified as the apparent surface. Here, d_1 is the interval between the first and second cation layers, that is the inner and outer sublayers of the crowded

20

layer, respectively. In this case, the reduced d_1 can be explained by the sequential arrangement of two cation layers and parallelly oriented cations in these layers.
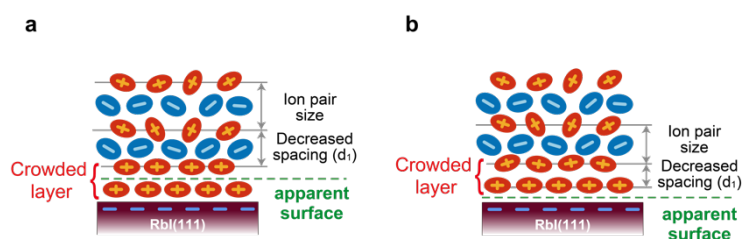

Figure 7. Two plausible models for solvation structures at IL/RbI(111) interfaces: (a) d_1 corresponds to the distance between the second and third cation layers, denoting the outer sublayers of the crowded layer and external cation layer, respectively. (b) d_1 is attributed to the distance between the first and second cation layers, denoting the inner and outer sublayers of the crowded layer, respectively.

The *crowding* model explains the decreased intensity of the solvation force peak at L_1 compared to L_2 at the IL/RbI(111) interfaces. Figure 8 presents a summary of layer counts and corresponding solvation force peaks extracted from short-range force profiles for RbI(100), mica and RbI(111) surfaces. The obtained solvation structures in both ILs on low-charged RbI(100) and moderately charged mica surfaces (approximately 20 $\mu C/cm^2$) show that higher surface charge densities lead to more pronounced solvation structures with stronger intensity of solvation force peaks and more layer counts. This suggests increased heterogeneity in ion density distribution perpendicular to the substrate with a higher surface charge density, which is consistent with prior simulation and experimental results.[11,21] However, this trend does not simply extend to the further higher surface charge density at RbI(111) surfaces (approximately 35 $\mu C/cm^2$). For example, in [C_3mpyr][Tf$_2$N], we observe that the solvation force peaks from L_2 to L_4 on RbI(111) closely resemble those on mica, yet L_1 on RbI(111) exhibits an apparently weaker solvation force peak than that on mica. One explanation is that the majority of surface charges on RbI(111) are counterbalanced by another layer of counterions (L_0), which is detected as the apparent surface (model shown in Figure 7a). Consequently, a similar solvation structure (associated with L_2 to L_4) was observed above the crowded layer on RbI(111) compared to mica.

Alternatively, if the model shown in Figure 7b is the case, consecutive two cation layers associated with L_1 and L_2 comprise a "thicker" innermost counterion layer. However, the solvation force peaks for this thick layer are unable to be compared directly with those applicable for *overscreening* model (the cases of RbI(100) and mica in this study).
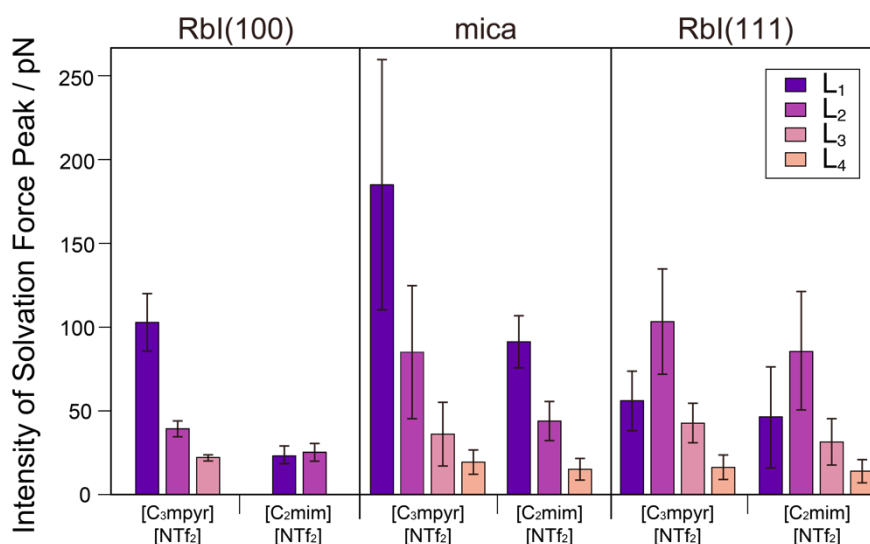

Figure 8. Intensity of solvation force peaks for solvation structures in [C$_3$mpyr][Tf$_2$N] and [C$_2$mim][Tf$_2$N] extracted from the short-range force profiles obtained on RbI(100), mica and RbI(111) surfaces. The error bars correspond to the standard error of the average for 6-10 data sets taken by the same tip for each interface.

At this point, identifying the actual model is difficult due to the resemblance in interatomic spacing on RbI(111) and the size of [C$_3$mpyr]$^+$ and [C$_2$mim]$^+$ cations. Two potential approaches are considered: first, employing ILs with bulkier cations; second, utilizing alkali halide(100) surfaces with smaller lattice constants. For instance, the NaCl(111) plane features an interatomic spacing of 0.397 nm, smaller than the dimensions of [C$_3$mpyr]$^+$ or [C$_2$mim]$^+$ cations used in this study. This implies that if a cation adsorption layer appears as the apparent surface, the high-resolution topographic image may reveal a lattice constant differing from the underlying substrate. Preparing an alkali halide(111) sample with a smaller lattice constant immersed in ILs might be potentially realized through the newly proposed IL-assisted vacuum deposition technique.[69,70] For instance, Matsumoto and colleagues have succeeded in growing

KBr(111) crystals on α-Al$_2$O$_3$(0001) substrate via this method.[69] However, despite its limitation to a single alkali halide(111) surface type, the proposed original preparation method is straightforward and does not require specialized equipment, potentially easing the exploration of ILs' response to high surface charge densities.

Response of Solvation Structures at IL/Solid Interfaces to Surface Charge Density

Employing FM-AFM with a qPlus sensor, we molecularly resolved the solvation structure of ILs on three surfaces with varied negative surface charge densities: RbI(100), mica, and RbI(111).

For RbI(100) with nearly zero surface charge densities, solvation structures comprised of alternating cation and anion layers were observed for both [C$_3$mpyr][Tf$_2$N] and [C$_2$mim][Tf$_2$N]. Previous SFG studies suggest that electrostatic interactions primarily drive the formation of solvation structures at IL/alkali halide(100) interfaces.[24] The observation of alternating cation and anion layers on RbI(100) surfaces in this study implies the occurrence of charge overcompensation at the interface.[71] Consequently, our data align with the idea that *overscreening* occurs at small surface charge densities close to zero, corroborating previous theoretical and simulation studies.[18,72]

The multilayer model for solvation structures at IL/alkali halide(100) interfaces would seem to contradict earlier SFG studies on imidazolium-based IL/NaCl(100) interfaces.[23,24,34] The authors observed that [C$_4$mim]$^+$ cations dominate NaCl(100) surfaces, and their imidazolium ring orients parallel to the substrate. On the other hand, anions exhibit an isotropic orientation. Accordingly, they proposed a Helmholtz-like single adsorption layer model, postulating that this monolayer effectively neutralizes the low surface charges of NaCl(100) surface.[23,24,34] This

discrepancy might stem from the different techniques applied. While SFG is sensitive to molecules in noncentrosymmetric environments,[24] FM-AFM offers greater sensitivity to spatial heterogeneity in molecule distribution at the interface. Recent studies combined AFM and MD simulation reveal that only ions adjacent to the substrate demonstrate significant orientation within multilayered solvation structures.[13,44] Therefore, the monolayer detected by SFG on NaCl(100) might present a Helmholtz-like structure or multilayers in which only the cations near the NaCl(100) surface are oriented. Earlier reviews have pointed out the possibility of a multilayered solvation structure at IL/alkali halide(100) interfaces,[3,73] albeit without any experimental evidence to support it. Our findings provide the first substantial evidence in support of this argument by molecularly resolving the multilayered solvation structures at various IL/alkali halide(100) interfaces.

Qualitative determination of the presence of monolayer or multilayer structures at IL/alkali halide(100) interfaces is essential. Kirchner *et al.* introduced a dimensionless surface-charge-compensation parameter κ_{ion} to describe the transition of solvation structures at IL/solid interfaces regarding surface charge density, which is expressed as $\kappa_{ion} = |\sigma/\theta_{max}|$ where σ is the solid surface charge density, and θ_{max} is the maximum charge density of a counterion monolayer.[74] They suggested that a transition from multilayer to monolayer structures occurs at $\kappa_{ion}=1$ and mentioned the possibility that the IL/NaCl(100) interface captures this transition.[74] Our data suggest that IL/alkali halide(100) interfaces more likely reflect the response of solvation structures to low surface charge densities rather than to the relatively high surface charge densities ($\kappa_{ion}=1$). This assumption is corroborated by the less pronounced solvation structure observed on RbI(100) compared to those on mica ($\kappa_{ion}<1$) in both ILs.

For highly charged RbI(111), our data (Figure 6) suggest the formation of crowded layers in both [C$_3$mpyr][Tf$_2$N] and [C$_2$mim][Tf$_2$N]. The fixed surface charge density on RbI(111) surface facilitate estimating κ_{ion}.[74] When $\kappa_{ion} > 1$, it is suggested that *crowding* occurs.[74] Recent fully atomistic simulation studies report that the θ_{max} for both [C$_4$mpyr]$^+$ and [C$_4$mim]$^+$ are around 45 μC/cm^2.[31,32] The authors also explored the effect of alkyl chain length on θ_{max} and found its effect is slight.[31] Therefore, we considered that the [C$_3$mpyr]$^+$ and [C$_2$mim]$^+$ cations used in this study likely have a similar θ_{max} compared to their counterparts with long alkyl chains. Using this value and the surface charge density of RbI(111), we estimated that κ_{ion} is approximately 0.8. Although the estimated κ_{ion} is larger than most IL/electrode systems,[32] it still falls below the anticipated threshold value ($\kappa_{ion} = 1$) for the onset of *crowding*. This contradiction may imply that the actual θ_{max} achievable by a single counterion layer might have been overestimated. A probable explanation could be that even when *crowding* occurs, the innermost layer is not solely composed of counterions, thus leading to a reduced θ_{max}. This assumption is corroborated by recent XRR studies, which have revealed that the crowded layer remains a mixture of counter and co-ions.[29,30]

Comparing the solvation structures of [C$_3$mpyr][Tf$_2$N] and [C$_2$mim][Tf$_2$N] on the same substrate surface, [C$_3$mpyr][Tf$_2$N] generally exhibits more pronounced solvation layers than [C$_2$mim][Tf$_2$N], as indicated by an increased layer count and stronger intensities of solvation force peaks. Since [C$_3$mpyr][Tf$_2$N] and [C$_2$mim][Tf$_2$N] share an identical anion, the difference in solvation structures likely originates from their cations, indicating that imidazolium-based ILs seemingly have superior screening abilities compared to their pyrrolidinium counterparts. Previous simulation studies have reported a similar result where dicyanamide [C$_4$mpyr][dca] exhibits the most prominent layering than [C$_2$mim][dca] and [C$_4$mim][dca] on negatively charged graphene surfaces.[75] A reasonable explanation is that the possible π-π stacking of

25

imidazolium rings enables cations to pack in a more efficient way to screen the surface charges.[75,76]

Conclusions

To understand the response of ILs' solvation structures to surface charge density, we proposed a new strategy by utilizing different facets of RbI crystals exhibiting varied surface charge densities: RbI(100) with near-zero surface charge densities, and RbI(111) with high surface charge densities which is typically beyond the reach of electrochemical systems. FM-AFM was employed to molecularly resolve the solvation structure of two commonly used ILs, $[C_3mpyr][Tf_2N]$ and $[C_2mim][Tf_2N]$, on these solid surfaces. On slightly charged RbI(100) surfaces, both ILs displayed multilayered solvation structures consisting of alternating cation and anion layers, suggesting that *overscreening* occurs at near-zero surface charge densities. These findings challenge the previously proposed Helmholtz-like monolayer model at IL/alkali halide(100) interfaces and highlight the significance of high-spatial-resolution techniques for characterizing IL interfacial structures. On the highly charged RbI(111) surfaces, both ILs presented crowded layers, consistent with theoretical predictions yet seldom observed in commonly used ILs. Given that crowding is not fully comprehended, the IL/alkali halide (111) interface may provide a novel avenue to explore the nanostructure and dynamics of ILs under high surface charge densities. The interfacial solvation structures elucidated in this study substantially advance our comprehension of IL/charged solid interfaces, potentially aiding in optimizing ILs for IL-based applications like supercapacitors, batteries, and lubricants.

26

Experimental Section

RbI(111) Sample Preparation

We propose a simple method to prepare rubidium iodide (RbI) crystals with (111) polar surfaces exposed. This method is based on the idea of heteroepitaxial growth of RbI crystals on a muscovite mica substrate in aqueous solutions.[38] We modify this method by using an RbI-dissolved IL solution. Since the solubility of alkali halide salt in ILs increases with temperature,[77] cooling crystallization is used to obtain RbI crystals.

[C$_3$mpyr][NTf$_2$] (> 98 %) and [C$_2$mim][NTf$_2$] (99.5 %) were purchased from Tokyo Chemical Industry Co., Ltd and Kanto Chemical Co., Inc, respectively. RbI powder (99.9%) was purchased from Sigma-Aldrich. 0.025 g of RbI powder was mixed with 1 mL of [C$_3$mpyr][NTf$_2$] and [C$_2$mim][NTf$_2$], respectively, to produce the corresponding RbI-saturated IL solutions under room temperature and at 378 K. The IL solutions were then heated at 378 K for 6 h on a hot plate within a dry chamber (dew point < 223 K, Daikin Industries, Ltd.), facilitating further dissolution of RbI powder and water removal. A muscovite mica (Furuuchi Chemical Co.) was preheated at 378 K for 10 min and cleaved using scotch tape to produce an atomically smooth, clean surface. Soon after cleavage, a droplet (0.5 µL) of the heated IL solution was placed onto the mica substrate, followed by cooling the sample to room temperature for crystallization. The entire process was performed within the dry chamber to minimize water content.

The charge density of the RbI(111) plane is around 69 µC/cm^2, determined from its lattice parameter. However, this polar surface is electrostatically unstable unless stabilized by compensating charges. In ILs, this stabilization could be achieved by the adsorption of IL ions.[70] The Tasker 1/2 rule suggests that the surface charge density σ_0 required to cancel by the

27

electrolyte ions should be -σ_0/2.[78] Accordingly, we estimate the effective surface charge density of RbI(111) to be approximately 35 µC/cm^2. Recent simulation studies have validated this theory by studying concentrated NaCl aqueous solution/NaCl(111) interfaces.[79]

RbI(100) Sample Preparation

We prepared RbI single crystals with exposed (100) surfaces by means of evaporation crystallization from aqueous solutions, followed by cleavage. 6.5 g of RbI powder was dissolved in 4 mL of ultrapure water (UPW, resistivity is 18.2 MΩ·cm). A crystal dish was pre-washed by ultrasonication in UPW and acetone (> 99.5 %, Nacalai Tesque, Inc.) for 10 min each. The RbI aqueous solution was transferred to the crystal dish and evaporated slowly to obtain RbI single crystals. RbI-saturated [C$_3$mpyr][NTf$_2$] and [C$_2$mim][NTf$_2$] solutions were previously heated at 378 K for 6 h on a hot plate within the dry chamber to remove water. Subsequently, droplets (0.2 µL) of cooled IL solutions were placed onto the freshly cleaved RbI(100) surface in the dry chamber.

Although alkali halide(100) surfaces are composed of equal numbers of cations and anions, surface rumpling results in a local field that is slightly charged nearly to zero.[24,28] Previous SFG studies have established that NaCl(100) surfaces tend to be slightly negatively charged in different types of imidazolium-based ILs.[23,24] Similarly, we propose that the RbI(100) surfaces are slightly charged in [C$_2$mim][NTf$_2$] and [C$_3$mpyr][NTf$_2$].This assumption is supported by a similar solvation structure observed at [C$_2$mim][NTf$_2$]/NaCl(100) interfaces compared with that on RbI(100) surfaces.

Muscovite mica substrate

Atomically smooth mica substrates were prepared by cleavage using a scotch tape. RbI-

saturated [C$_3$mpyr][NTf$_2$] and [C$_2$mim][NTf$_2$] solutions were previously heated at 378 K for 6 hours on a hot plate within the dry chamber to remove water. Next, the droplets of cooled RbI-saturated IL solutions were dropped on the freshly cleaved mica surface. All the process was performed in the dry chamber.

The mica(001) surface acquires negative charges in solutions with high dielectric constants due to the desorption of K$^+$ ions. These ions neutralize the negative charges arising from the random substitution of a quarter of Si^{4+} ions by Al^{3+} ions in the bulk phase. Consequently, its surface charge density can vary from 0 (with K$^+$ ions retained on the surface) to approximately 32 μC/cm^2 (when K$^+$ ions are fully desorbed into the ILs).[11] A recent study determined that the typical surface charge density of mica in ILs is about -20 μC/cm^2.[35] This was done by comparing the force between [C$_2$mim][NTf$_2$]/mica and [C$_2$mim][NTf$_2$]/biased gold interfaces,[35] which is the same IL as in our study. Here, we use this value as a reference.

X-ray diffraction (XRD) analysis

The XRD patterns of RbI crystals grown on mica substrate, and RbI crystals by the evaporation crystallization were obtained using a diffractometer (X'Pert PRO Alpha-1, PANalytical) at 40 kV and 10 mA with a Cu radiation source. The obtained data were processed using Igor software.

Atomic force microscopy (AFM) observation

All AFM observations were performed in the FM mode using a commercial AFM (JSPM-5200, JEOL) with some modifications.[80] The original head of the AFM was replaced by a custom-built one for a qPlus sensor.[80] The qPlus sensor was prepared as follows: We fixed a quartz tuning fork (QTF, SII Crystal Technology Inc.) onto a substrate, followed by gluing a

tungsten tip to one prong of the QTF.[81] The tungsten tip was prepared from tungsten wires (Φ = 0.1 mm, Nilaco Co.) by electrochemical etching in a 1.2 mol·L^{-1} potassium hydroxide solution. The typical resonance frequency (f_0) and spring constant of the QTF are 32.768 kHz and 1.9×10^3 N·m^{-1} before being glued by a tungsten tip. The sensor was mechanically vibrated by the zirconate titanate piezoelectric plate, and its deflection signal was detected by a differential current pre-amplifier embedded in the AFM head.[82] A commercially available phase-locked loop circuit based on a digital lock-in amplifier (MFLI 500 kHz, Zurich Instruments) was used to detect shifts in the resonance frequency (Δf) of the sensor and keep its amplitude constant during scanning.

This study used AFM for topographic imaging and two-dimensional (2D) frequency shift (Δf) mapping measurements. Topographic images were obtained by presenting the in-plane (x-y plane) tip trajectories along the substrate surface during scanning while keeping Δf constant. The obtained AFM topographic images were processed with WSxM software.[83]All the high-resolution AFM images are shown after the drift correction by comparing the two consecutively taken images with opposite slow scan directions, except the Figure S3e where square lattices are not severely distorted by drift.

2D Δf mapping was performed as follows: The tip-to-sample distance was changed without Δf feedback while the tip was kept at the same place in the x-y plane. Then the tip changed its lateral position and repeated the same measurement. The obtained 2D Δf maps were processed using Igor software and sheared to reduce the effect of thermal drift. The contrasts of the 2D maps are adjusted to visually enhance the fine details associated with solvation structures. Since the minimum Δf for obtaining atomic resolution imaging is 10 Hz (Figure 2l), we adjusted the maximum for the maps' contrast to 10 Hz, which is remarked as the grey-colored

featureless regions for convenience.

Schematic illustration

The schematic illustrations of RbI crystal structure were processed using VESTA software,[84] and those of molecular structures of ILs were processed using Avogadro software.[85]

ASSOCIATED CONTENT

Supporting Information

(a) Successive AFM topographic images of RbI(111) surfaces in $[C_3mpyr][NTf_2]$.

(b) Force versus tip-to-sample distance profiles converted from frequency shift versus tip-to-sample distance profiles.

(c) The intensity of solvation force peak extracted from the short-range force profiles.

(d) AFM results obtained at the $[C_3mpyr][NTf_2]/NaCl(100)$ interface.

(e) AFM results obtained at the $[C_2mim][NTf_2]/NaCl(100)$ interface.

(f) 2D dissipation maps simultaneously obtained with frequency shift maps at $[C_3mpyr][NTf_2]/RbI(111)$ and $[C_2mim][NTf_2]/RbI(111)$ interfaces.

Author Information

Corresponding Author

Takashi Ichii

Department of Materials Science and Engineering,

Graduate School of Engineering,

Kyoto University, Kyoto 606-8501, Japan

Email address: ichii.takashi.2m@kyoto-u.ac.jp

Fax: +81-75-753-5484
Tel: +81-75-753-9132

Author

Yifan Bao, *Department of Materials Science and Engineering, Kyoto University, Yoshida-Honmachi, Sakyo-ku, Kyoto, 606-8501, Japan*
https://orcid.org/0009-0004-7253-8149

Yuto Nishiwaki, *Department of Materials Science and Engineering, Kyoto University, Yoshida-Honmachi, Sakyo-ku, Kyoto, 606-8501, Japan*
https://orcid.org/0009-0002-9550-326X

Touma Kawano, *Department of Materials Science and Engineering, Kyoto University, Yoshida-Honmachi, Sakyo-ku, Kyoto, 606-8501, Japan*

Toru Utsunomiya, *Department of Materials Science and Engineering, Kyoto University, Yoshida-Honmachi, Sakyo-ku, Kyoto, 606-8501, Japan*
https://orcid.org/0000-0002-0023-7812

Hiroyuki Sugimura, *Department of Materials Science and Engineering, Kyoto University, Yoshida-Honmachi, Sakyo-ku, Kyoto, 606-8501, Japan*
https://orcid.org/0000-0002-6415-8558

Takashi Ichii, *Department of Materials Science and Engineering, Kyoto University, Yoshida-Honmachi, Sakyo-ku, Kyoto, 606-8501, Japan*
https://orcid.org/0000-0002-4021-8894

Author Contributions

T. I., Y. B. and T. U. designed the whole project. T. I., T. U., H. S. supervised the project. T. I. developed the AFM equipment. Y. B. and T. K. and Y. N. performed the experiments. Y. B. drafted the original manuscript. All authors contributed to the interpretation of the results and preparation of the manuscript.

Notes

The authors declare no competing financial interest.

Acknowledgements

Reference

(1)   Endres, F.; Zein El Abedin, S. Air and Water Stable Ionic Liquids in Physical Chemistry. *Physical Chemistry Chemical Physics* **2006**, *8* (18), 2101–2116. https://doi.org/10.1039/b600519p.

(2)   Weingärtner, H. Understanding Ionic Liquids at the Molecular Level: Facts, Problems, and Controversies. *Angewandte Chemie International Edition* **2008**, *47* (4), 654–670. https://doi.org/10.1002/anie.200604951.

(3)   Hayes, R.; Warr, G. G.; Atkin, R. Structure and Nanostructure in Ionic Liquids. *Chem. Rev.* **2015**, *115* (13), 6357–6426. https://doi.org/10.1021/cr500411q.

(4)   Rogers, R. D.; Seddon, K. R. Ionic Liquids--Solvents of the Future? *Science* **2003**, *302* (5646), 792–793. https://doi.org/10.1126/science.1090313.

(5)   Endres, F. Ionic Liquids: Solvents for the Electrodeposition of Metals and Semiconductors. *Physical Chemistry Chemical Physics* **2002**, *3* (2), 144–154. https://doi.org/10.1002/1439-7641(20020215)3:2<144::AID-CPHC144>3.0.CO;2-%23

(6)   Wang, X.; Salari, M.; Jiang, D.; Chapman Varela, J.; Anasori, B.; Wesolowski, D. J.; Dai, S.; Grinstaff, M. W.; Gogotsi, Y. Electrode Material–Ionic Liquid Coupling for Electrochemical Energy Storage. *Nat. Rev. Mater.* **2020**, *5* (11), 787–808. https://doi.org/10.1038/s41578-020-0218-9.

(7)   Bresme, F.; Kornyshev, A. A.; Perkin, S.; Urbakh, M. Electrotunable Friction with Ionic Liquid Lubricants. *Nat. Mater.* **2022**, *21* (8), 848–858. https://doi.org/10.1038/s41563-022-01273-7.

(8)   Ivanistsev, V.; Fedorov, M. V. Interfaces between Charged Surfaces and Ionic Liquids: Insights from Molecular Simulations. *Electrochem. Soc. Interface.* **2014**, *23* (1), 65–69. https://doi.org/10.1149/2.F08141if.

(9)   Fedorov, M. V.; Kornyshev, A. A. Ionic Liquids at Electrified Interfaces. *Chem. Rev.* **2014**, *114* (5), 2978–3036. https://doi.org/10.1021/cr400374x.

(10) Mezger, M.; Schröder, H.; Reichert, H.; Schramm, S.; Okasinski, J. S.; Schöder, S.; Honkimäki, V.; Deutsch, M.; Ocko, B. M.; Ralston, J.; Rohwerder, M.; Stratmann, M.; Dosch, H. Molecular Layering of Fluorinated Ionic Liquids at a Charged Sapphire (0001) Surface. *Science* **2008**, *322* (5900), 424–428. https://doi.org/10.1126/science.1164502.

(11) Zhou, H.; Rouha, M.; Feng, G.; Lee, S. S.; Docherty, H.; Fenter, P.; Cummings, P. T.; Fulvio, P. F.; Dai, S.; McDonough, J.; Presser, V.; Gogotsi, Y. Nanoscale Perturbations of Room Temperature Ionic Liquid Structure at Charged and Uncharged Interfaces. *ACS Nano* **2012**, *6* (11), 9818–9827. https://doi.org/10.1021/nn303355b.

(12) Nishi, N.; Uchiyashiki, J.; Ikeda, Y.; Katakura, S.; Oda, T.; Hino, M.; Yamada, N. L. Potential-Dependent Structure of the Ionic Layer at the Electrode Interface of an Ionic Liquid Probed Using Neutron Reflectometry. *Journal of Physical Chemistry C* **2019**, *123* (14), 9223–9230. https://doi.org/10.1021/acs.jpcc.9b01151.

(13) Black, J. M.; Walters, D.; Labuda, A.; Feng, G.; Hillesheim, P. C.; Dai, S.; Cummings, P. T.; Kalinin, S. V.; Proksch, R.; Balke, N. Bias-Dependent Molecular-Level Structure of Electrical Double Layer in Ionic Liquid on Graphite. *Nano Lett.* **2013**, *13* (12), 5954–5960. https://doi.org/10.1021/nl4031083.

(14) Mao, X.; Brown, P.; Červinka, C.; Hazell, G.; Li, H.; Ren, Y.; Chen, D.; Atkin, R.; Eastoe, J.; Grillo, I.; Padua, A. A. H.; Costa Gomes, M. F.; Hatton, T. A. Self-Assembled Nanostructures in Ionic Liquids Facilitate Charge Storage at Electrified Interfaces. *Nat. Mater.* **2019**, *18* (12), 1350–1357. https://doi.org/10.1038/s41563-019-0449-6.

(15) Umeda, K.; Kobayashi, K.; Minato, T.; Yamada, H. Molecular-Scale Solvation Structures of Ionic Liquids on a Heterogeneously Charged Surface. *Journal of Physical Chemistry Letters* **2020**, *11* (19), 8094–8099. https://doi.org/10.1021/acs.jpclett.0c02356.

(16) Rakov, D. A.; Chen, F.; Ferdousi, S. A.; Li, H.; Pathirana, T.; Simonov, A. N.; Howlett, P. C.; Atkin, R.; Forsyth, M. Engineering High-Energy-Density Sodium Battery Anodes for Improved Cycling with Superconcentrated Ionic-Liquid Electrolytes. *Nat. Mater.* **2020**, *19* (10), 1096–1101. https://doi.org/10.1038/s41563-020-0673-0.

(17) Smith, A. M.; Lovelock, K. R. J.; Gosvami, N. N.; Licence, P.; Dolan, A.; Welton, T.; Perkin, S. Monolayer to Bilayer Structural Transition in Confined Pyrrolidinium-Based Ionic Liquids. *J. Phys. Chem. Lett.* **2013**, *4* (3), 378–382. https://doi.org/10.1021/jz301965d.

(18) Bazant, M. Z.; Storey, B. D.; Kornyshev, A. A. Double Layer in Ionic Liquids: Overscreening versus Crowding. *Phys. Rev. Lett.* **2011**, *106* (4), 046102. https://doi.org/10.1103/PhysRevLett.106.046102.

(19) Kornyshev, A. A. Double-Layer in Ionic Liquids: Paradigm Change? *Journal of Physical Chemistry B* **2007**, *111* (20), 5545–5557. https://doi.org/10.1021/jp067857o.

(20) Zhang, X.; Zhong, Y.-X.; Yan, J.-W.; Su, Y.-Z.; Zhang, M.; Mao, B.-W. Probing Double Layer Structures of Au(111)–BMIPF$_6$ Ionic Liquid Interfaces from Potential-Dependent AFM Force Curves. *Chem. Commun.* **2012**, *48* (4), 582–584. https://doi.org/10.1039/C1CC15463J.

(21) Uysal, A.; Zhou, H.; Feng, G.; Lee, S. S.; Li, S.; Fenter, P.; Cummings, P. T.; Fulvio, P. F.; Dai, S.; McDonough, J. K.; Gogotsi, Y. Structural Origins of Potential Dependent Hysteresis at the Electrified Graphene/Ionic Liquid Interface. *The Journal of Physical Chemistry C* **2014**, *118* (1), 569–574. https://doi.org/10.1021/jp4111025.

(22) Zhong, Y.-X.; Yan, J.-W.; Li, M.-G.; Zhang, X.; He, D.-W.; Mao, B.-W. Resolving Fine Structures of the Electric Double Layer of Electrochemical Interfaces in Ionic Liquids with an AFM Tip Modification Strategy. *J. Am. Chem. Soc.* **2014**, *136* (42), 14682–14685. https://doi.org/10.1021/ja508222m.

(23) Peñalber, C. Y.; Baker, G. A.; Baldelli, S. Sum Frequency Generation Spectroscopy of Imidazolium-Based Ionic Liquids with Cyano-Functionalized Anions at the Solid Salt-Liquid Interface. *Journal of Physical Chemistry B* **2013**, *117* (19), 5939–5949. https://doi.org/10.1021/jp4019074.

(24) Peñalber, C. Y.; Baldelli, S. Observation of Charge Inversion of an Ionic Liquid at the Solid Salt-Liquid Interface by Sum Frequency Generation Spectroscopy. *Journal of Physical Chemistry Letters* **2012**, *3* (7), 844–847. https://doi.org/10.1021/jz3000917.

(25) Mungse, H. P.; Okudaira, S.; Yamauchi, M.; Ichii, T.; Utsunomiya, T.; Maruyama, S.; Matsumoto, Y.; Sugimura, H. Surface Charge Dependent Structure of Ionic Liquid/Alkali Halide Interfaces Investigated by Atomic Force Microscopy. *Jpn. J. Appl. Phys.* **2022**, *61* (SL), SL1009. https://doi.org/10.35848/1347-4065/ac528e.

(26) Belotti, M.; Lyu, X.; Xu, L.; Halat, P.; Darwish, N.; Silvester, D. S.; Goh, C.; Izgorodina, E. I.; Coote, M. L.; Ciampi, S. Experimental Evidence of Long-Lived Electric Fields of Ionic Liquid Bilayers. *J. Am. Chem. Soc.* **2021**, *143* (42), 17431–17440. https://doi.org/10.1021/jacs.1c06385.

(27) Vogt, J. Tensor LEED Study of the Temperature Dependent Dynamics of the NaCl(100) Single Crystal Surface. *Phys. Rev. B.* **2007**, *75* (12), 125423. https://doi.org/10.1103/PhysRevB.75.125423.

(28) Vogt, J.; Weiss, H. The Structure of NaCl(100) and KCl(100) Single Crystal Surfaces: A Tensor Low Energy Electron Diffraction Analysis. *Surf. Sci.* **2001**, *491* (1–2), 155–168. https://doi.org/10.1016/S0039-6028(01)01391-7.

(29) Chu, M.; Miller, M.; Dutta, P. Crowding and Anomalous Capacitance at an Electrode-Ionic Liquid Interface Observed Using Operando X-Ray Scattering. *ACS Cent. Sci.* **2016**, *2* (3), 175–180. https://doi.org/10.1021/acscentsci.6b00014.

(30) Douglas, T.; Yoo, S.; Dutta, P. Ionic Liquid Solutions Show Anomalous Crowding Behavior at an Electrode Surface. *Langmuir* **2022**, *38* (20), 6322–6329. https://doi.org/10.1021/acs.langmuir.2c00036.

(31) Karu, K.; Nerut, E. R.; Tao, X.; Kislenko, S. A.; Pohako-Esko, K.; Voroshylova, I. V.; Ivaništšev, V. B. Ionic Liquid-Electrode Interface: Classification of Ions, Saturation of Layers, and Structure-Determined Potentials. *arXiv preprint* **2023**. https://doi.org/10.48550/arXiv.2302.00076.

(32) Kislenko, S. A.; Moroz, Y. O.; Karu, K.; Ivaništšev, V. B.; Fedorov, M. V. Calculating the Maximum Density of the Surface Packing of Ions in Ionic Liquids. *Russian Journal*

of Physical Chemistry A **2018**, *92* (5), 999–1005. https://doi.org/10.1134/S0036024418050187.

(33) Watanabe, S.; Pilkington, G. A.; Oleshkevych, A.; Pedraz, P.; Radiom, M.; Welbourn, R.; Glavatskih, S.; Rutland, M. W. Interfacial Structuring of Non-Halogenated Imidazolium Ionic Liquids at Charged Surfaces: Effect of Alkyl Chain Length. *Physical Chemistry Chemical Physics* **2020**, *22* (16), 8450–8460. https://doi.org/10.1039/d0cp00360c.

(34) Baldelli, S. Interfacial Structure of Room-Temperature Ionic Liquids at the Solid-Liquid Interface as Probed by Sum Frequency Generation Spectroscopy. *Journal of Physical Chemistry Letters* **2013**, *4* (2), 244–252. https://doi.org/10.1021/jz301835j.

(35) Coles, S. W.; Smith, A. M.; Fedorov, M. V.; Hausen, F.; Perkin, S. Interfacial Structure and Structural Forces in Mixtures of Ionic Liquid with a Polar Solvent. *Faraday Discuss.* **2018**, *206*, 427–442. https://doi.org/10.1039/c7fd00168a.

(36) Ichii, T.; Itakura, K.; Bao, Y.; Utsunomiya, T.; Sugimura, H. Two-Dimensional Analysis on Interfacial Solvation Structure of Ionic Liquid Electrolyte on a Hydrogen-Terminated Si Electrode by Atomic Force Microscopy. *Jpn. J. Appl. Phys.* **2024**, *63* (5), 05SP18. https://doi.org/10.35848/1347-4065/ad41eb.

(37) Bao, Y.; Kitta, M.; Ichii, T.; Utsunomiya, T.; Sugimura, H. Visualization of Solvation Structure on $Li_4Ti_5O_{12}$(111)/ Ionic Liquid-Based Electrolyte Interface by Atomic Force Microscopy. *Jpn. J. Appl. Phys.* **2021**, *60* (SE), SE1004. https://doi.org/10.35848/1347-4065/abf3a3.

(38) Lamelas, F.; Schmidt, J.; Xiong, M. Heteroepitaxial Growth in Aqueous Solutions: Rubidium Iodide on Mica. *Phys. Rev. B* **1998**, *58* (21), 14270–14278. https://doi.org/10.1103/PhysRevB.58.14270.

(39) Lamelas, F. J.; Xiong, M.; Sloane, C. V. Crystallographic Tilting during Heteroepitaxial Growth of Rubidium Iodide on Mica. *Phys. Rev. B* **2000**, *62* (12), 8330–8337. https://doi.org/10.1103/PhysRevB.62.8330.

(40) Soo Lee, S.; Koishi, A.; Bourg, I. C.; Fenter, P. Ion Correlations Drive Charge Overscreening and Heterogeneous Nucleation at Solid-Aqueous Electrolyte Interfaces. *Proceedings of the National Academy of Sciences* **2021**, *118* (32), e2105154118. https://doi.org/10.1073/pnas.2105154118/-/DCSupplemental.

(41) Wen, R.; Rahn, B.; Magnussen, O. M. Potential-Dependent Adlayer Structure and Dynamics at the Ionic Liquid/Au(111) Interface: A Molecular-Scale in Situ Video-STM Study. *Angewandte Chemie International Edition* **2015**, *54* (20), 6062–6066. https://doi.org/10.1002/anie.201501715.

(42) Sheehan, A.; Jurado, L. A.; Ramakrishna, S. N.; Arcifa, A.; Rossi, A.; Spencer, N. D.; Espinosa-Marzal, R. M. Layering of Ionic Liquids on Rough Surfaces. *Nanoscale* **2016**, *8* (7), 4094–4106. https://doi.org/10.1039/c5nr07805a.

(43) Zhou, S.; Panse, K. S.; Motevaselian, M. H.; Aluru, N. R.; Zhang, Y. Three-Dimensional Molecular Mapping of Ionic Liquids at Electrified Interfaces. *ACS Nano* **2020**, *14* (12), 17515–17523. https://doi.org/10.1021/acsnano.0c07957.

(44) Panse, K. S.; Wu, H.; Zhou, S.; Zhao, F.; Aluru, N. R.; Zhang, Y. Innermost Ion Association Configuration Is a Key Structural Descriptor of Ionic Liquids at Electrified Interfaces. *Journal of Physical Chemistry Letters* **2022**, *13* (40), 9464–9472. https://doi.org/10.1021/acs.jpclett.2c02768.

(45) Bonagiri, L. K. S.; Panse, K. S.; Zhou, S.; Wu, H.; Aluru, N. R.; Zhang, Y. Real-Space Charge Density Profiling of Electrode-Electrolyte Interfaces with Angstrom Depth Resolution. *ACS Nano* **2022**, *16* (11), 19594–19604. https://doi.org/10.1021/acsnano.2c10819.

(46) Ito, F.; Kobayashi, K.; Spijker, P.; Zivanovic, L.; Umeda, K.; Nurmi, T.; Holmberg, N.; Laasonen, K.; Foster, A. S.; Yamada, H. Molecular Resolution of the Water Interface at an Alkali Halide with Terraces and Steps. *Journal of Physical Chemistry C* **2016**, *120* (35), 19714–19722. https://doi.org/10.1021/acs.jpcc.6b05651.

(47) Arai, T.; Koshioka, M.; Abe, K.; Tomitori, M.; Kokawa, R.; Ohta, M.; Yamada, H.; Kobayashi, K.; Oyabu, N. Atom-Resolved Analysis of an Ionic KBr(001) Crystal Surface Covered with a Thin Water Layer by Frequency Modulation Atomic Force Microscopy. *Langmuir* **2015**, *31* (13), 3876–3883. https://doi.org/10.1021/acs.langmuir.5b00087.

(48) Ichii, T.; Negami, M.; Sugimura, H. Atomic-Resolution Imaging on Alkali Halide Surfaces in Viscous Ionic Liquid Using Frequency Modulation Atomic Force Microscopy. *Journal of Physical Chemistry C* **2014**, *118* (46), 26803–26807. https://doi.org/10.1021/jp5078505.

(49) Hoffmann, R.; Kantorovich, L. N.; Baratoff, A.; Hug, H. J.; Güntherodt, H. J. Sublattice Identification in Scanning Force Microscopy on Alkali Halide Surfaces. *Phys. Rev. Lett.* **2004**, *92* (14), 146103. https://doi.org/10.1103/PhysRevLett.92.146103.

(50) Perkin, S.; Crowhurst, L.; Niedermeyer, H.; Welton, T.; Smith, A. M.; Gosvami, N. N. Self-Assembly in the Electrical Double Layer of Ionic Liquids. *Chemical Communications* **2011**, *47* (23), 6572. https://doi.org/10.1039/c1cc11322d.

(51) Chen, N.; Li, Y.; Dai, Y.; Qu, W.; Xing, Y.; Ye, Y.; Wen, Z.; Guo, C.; Wu, F.; Chen, R. A Li^+ Conductive Metal Organic Framework Electrolyte Boosts the High-Temperature Performance of Dendrite-Free Lithium Batteries. *J. Mater. Chem. A* **2019**, *7* (16), 9530–9536. https://doi.org/10.1039/c8ta12539b.

(52) Black, J. M.; Zhu, M.; Zhang, P.; Unocic, R. R.; Guo, D.; Okatan, M. B.; Dai, S.; Cummings, P. T.; Kalinin, S. V.; Feng, G.; Balke, N. Fundamental Aspects of Electric Double Layer Force-Distance Measurements at Liquid-Solid Interfaces Using Atomic Force Microscopy. *Sci. Rep.* **2016**, *6*, 32389. https://doi.org/10.1038/srep32389.

(53) Uhlig, M. R.; Martin-Jimenez, D.; Garcia, R. Atomic-Scale Mapping of Hydrophobic Layers on Graphene and Few-Layer MoS2 and WSe2 in Water. *Nat. Commun.* **2019**, *10* (1), 2606. https://doi.org/10.1038/s41467-019-10740-w.

(54) Sader, J. E.; Jarvis, S. P. Accurate Formulas for Interaction Force and Energy in Frequency Modulation Force Spectroscopy. *Appl. Phys. Lett.* **2004**, *84* (10), 1801–1803. https://doi.org/10.1063/1.1667267.

(55) Kilpatrick, J. I.; Loh, S. H.; Jarvis, S. P. Directly Probing the Effects of Ions on Hydration Forces at Interfaces. *J. Am. Chem. Soc.* **2013**, *135* (7), 2628–2634. https://doi.org/10.1021/ja310255s.

(56) Utsunomiya, T.; Yokota, Y.; Enoki, T.; Fukui, K. I. Potential-Dependent Hydration Structures at Aqueous Solution/Graphite Interfaces by Electrochemical Frequency Modulation Atomic Force Microscopy. *Chemical Communications* **2014**, *50* (98), 15537–15540. https://doi.org/10.1039/c4cc07093c.

(57) Umeda, K.; Kobayashi, K.; Minato, T.; Yamada, H. Atomic-Scale Three-Dimensional Local Solvation Structures of Ionic Liquids. *J. Phys. Chem. Lett.* **2020**, *11* (4), 1343–1348. https://doi.org/10.1021/acs.jpclett.9b03874.

(58) Horn, R. G.; Evans, D. F.; Ninham, B. W. Double-Layer and Solvation Forces Measured in a Molten Salt and Its Mixtures with Water. *J. Phys. Chem.* **1988**, *92* (12), 3531–3537. https://doi.org/10.1021/j100323a042.

(59) Watkins, M.; Reischl, B. A Simple Approximation for Forces Exerted on an AFM Tip in Liquid. *Journal of Chemical Physics* **2013**, *138* (15), 154703. https://doi.org/10.1063/1.4800770.

(60) Amano, K. I.; Suzuki, K.; Fukuma, T.; Takahashi, O.; Onishi, H. The Relationship between Local Liquid Density and Force Applied on a Tip of Atomic Force Microscope: A Theoretical Analysis for Simple Liquids. *Journal of Chemical Physics* **2013**, *139* (22), 224710. https://doi.org/10.1063/1.4839775.

(61) Miyazawa, K.; Kobayashi, N.; Watkins, M.; Shluger, A. L.; Amano, K. I.; Fukuma, T. A Relationship between Three-Dimensional Surface Hydration Structures and Force Distribution Measured by Atomic Force Microscopy. *Nanoscale* **2016**, *8* (13), 7334–7342. https://doi.org/10.1039/c5nr08092d.

(62) Amano, K. I.; Yokota, Y.; Ichii, T.; Yoshida, N.; Nishi, N.; Katakura, S.; Imanishi, A.; Fukui, K. I.; Sakka, T. A Relationship between the Force Curve Measured by Atomic Force Microscopy in an Ionic Liquid and Its Density Distribution on a Substrate. *Physical Chemistry Chemical Physics* **2017**, *19* (45), 30504–30512. https://doi.org/10.1039/c7cp06948k.

(63) Benaglia, S.; Uhlig, M. R.; Hernández-Muñoz, J.; Chacón, E.; Tarazona, P.; Garcia, R. Tip Charge Dependence of Three-Dimensional AFM Mapping of Concentrated Ionic Solutions. *Phys. Rev. Lett.* **2021**, *127* (19), 196101. https://doi.org/10.1103/PhysRevLett.127.196101.

(64) Suzuk, T.; Yamada, Y. Dispersion and Polar Component of Specific Surface Free Energy of NaCl(100), KCl(100), and KBr(100) Single Crystal Surfaces. *Journal of Crystallization Process and Technology* **2015**, *05* (03), 43–47. https://doi.org/10.4236/jcpt.2015.53006.

(65) Okaue, D.; Tanabe, I.; Ono, S.; Sakamoto, K.; Sato, T.; Imanishi, A.; Morikawa, Y.; Takeya, J.; Fukui, K. I. Ionic-Liquid-Originated Carrier Trapping Dynamics at the Interface in Electric Double-Layer Organic FET Revealed by Operando Interfacial Analyses. *Journal of Physical Chemistry C* **2020**, *124* (4), 2543–2552. https://doi.org/10.1021/acs.jpcc.9b10636.

(66) Hofbauer, W.; Ho, R. J.; Hairulnizam, R.; Gosvami, N. N.; O'Shea, S. J. Crystalline Structure and Squeeze-out Dissipation of Liquid Solvation Layers Observed by Small-Amplitude Dynamic AFM. *Phys. Rev. B* **2009**, *80* (13). https://doi.org/10.1103/PhysRevB.80.134104.

(67) Yamada, Y.; Ichii, T.; Utsunomiya, T.; Sugimura, H. Visualizing Polymeric Liquid/Solid Interfaces by Atomic Force Microscopy Utilizing Quartz Tuning Fork Sensors. *Jpn. J. Appl. Phys.* **2020**, *59*, SN1009. https://doi.org/10.35848/1347-4065/ab84b0.

(68) Lahiri, A.; Carstens, T.; Atkin, R.; Borisenko, N.; Endres, F. In Situ Atomic Force Microscopic Studies of the Interfacial Multilayer Nanostructure of LiTFSI-[Py1, 4]TFSI on Au(111): Influence of Li$^+$ Ion Concentration on the Au(111)/IL Interface. *Journal of Physical Chemistry C* **2015**, *119* (29), 16734–16742. https://doi.org/10.1021/acs.jpcc.5b04562.

(69) Yamauchi, M.; Maruyama, S.; Ohashi, N.; Toyabe, K.; Matsumoto, Y. Epitaxial Growth of Atomically Flat KBr(111) Films: Via a Thin Film Ionic Liquid in a Vacuum. *Cryst. Eng. Comm.* **2016**, *18* (19), 3399–3403. https://doi.org/10.1039/c6ce00620e.

(70) Kato, S.; Takeyama, Y.; Maruyama, S.; Matsumoto, Y. Nonfaceted Growth of (111)-Oriented Epitaxial Alkali-Halide Crystals via an Ionic Liquid Flux in a Vacuum. *Cryst. Growth. Des.* **2010**, *10* (8), 3608–3611. https://doi.org/10.1021/cg100493t.

(71) Gil, P. S.; Jorgenson, S. J.; Riet, A. R.; Lacks, D. J. Relationships between Molecular Structure, Interfacial Structure, and Dynamics of Ionic Liquids near Neutral and Charged Surfaces. *Journal of Physical Chemistry C* **2018**, *122* (48), 27462–27468. https://doi.org/10.1021/acs.jpcc.8b08644.

(72) Fedorov, M. V.; Kornyshev, A. A. Towards Understanding the Structure and Capacitance of Electrical Double Layer in Ionic Liquids. *Electrochim. Acta* **2008**, *53* (23), 6835–6840. https://doi.org/10.1016/j.electacta.2008.02.065.

(73) Vatamanu, J.; Bedrov, D. Capacitive Energy Storage: Current and Future Challenges. *Journal of Physical Chemistry Letters* **2015**, *6* (18), 3594–3609. https://doi.org/10.1021/acs.jpclett.5b01199.

(74) Kirchner, K.; Kirchner, T.; Ivaništšev, V.; Fedorov, M. V. Electrical Double Layer in Ionic Liquids: Structural Transitions from Multilayer to Monolayer Structure at the Interface. *Electrochim. Acta* **2013**, *110*, 762–771. https://doi.org/10.1016/j.electacta.2013.05.049.

(75) Begić, S.; Jónsson, E.; Chen, F.; Forsyth, M. Molecular Dynamics Simulations of Pyrrolidinium and Imidazolium Ionic Liquids at Graphene Interfaces. *Physical Chemistry Chemical Physics* **2017**, *19* (44), 30010–30020. https://doi.org/10.1039/c7cp03389c.

(76) Begić, S. S. D.; Chen, F.; Jónsson, E.; Forsyth, M. Overscreening and Crowding in Electrochemical Ionic Liquid Systems. *Phys. Rev. Mater.* **2019**, *3* (9), 095801. https://doi.org/10.1103/PhysRevMaterials.3.095801.

(77) Kuzmina, O.; Bordes, E.; Schmauck, J.; Hunt, P. A.; Hallett, J. P.; Welton, T. Solubility of Alkali Metal Halides in the Ionic Liquid [C$_4$C$_1$im][OTf]. *Physical Chemistry Chemical Physics* **2016**, *18* (24), 16161–16168. https://doi.org/10.1039/c6cp02286c.

(78) Tasker, P. W. The Stability of Ionic Crystal Surfaces. *Journal of Physics C: Solid State Physics* **1979**, *12* (22), 4977–4984. https://doi.org/10.1088/0022-3719/12/22/036.

(79) Sayer, T.; Zhang, C.; Sprik, M. Charge Compensation at the Interface between the Polar NaCl(111) Surface and a NaCl Aqueous Solution. *Journal of Chemical Physics* **2017**, *147* (10). https://doi.org/10.1063/1.4987019.

(80) Ichii, T.; Fujimura, M.; Negami, M.; Murase, K.; Sugimura, H. Frequency Modulation Atomic Force Microscopy in Ionic Liquid Using Quartz Tuning Fork Sensors. *Jpn. J. Appl. Phys.* **2012**, *51* (8S3), 08KB08. https://doi.org/10.1143/JJAP.51.08KB08.

(81) Giessibl, F. J. High-Speed Force Sensor for Force Microscopy and Profilometry Utilizing a Quartz Tuning Fork. *Appl. Phys. Lett.* **1998**, *73* (26), 3956–3958. https://doi.org/10.1063/1.122948.

(82) Huber, F.; Giessibl, F. J. Low Noise Current Preamplifier for QPlus Sensor Deflection Signal Detection in Atomic Force Microscopy at Room and Low Temperatures. *Review of Scientific Instruments* **2017**, *88* (7), 073702. https://doi.org/10.1063/1.4993737.

(83) Horcas, I.; Fernández, R.; Gómez-Rodríguez, J. M.; Colchero, J.; Gómez-Herrero, J.; Baro, A. M. WSXM: A Software for Scanning Probe Microscopy and a Tool for Nanotechnology. *Review of Scientific Instruments* **2007**, *78* (1), 013705. https://doi.org/10.1063/1.2432410.

(84) Momma, K.; Izumi, F. VESTA 3 for Three-Dimensional Visualization of Crystal, Volumetric and Morphology Data. *J. Appl. Crystallogr.* **2011**, *44* (6), 1272–1276. https://doi.org/10.1107/S0021889811038970.

(85) Hanwell, M. D.; Curtis, D. E.; Lonie, D. C.; Vandermeersch, T.; Zurek, E.; Hutchison, G. R. Avogadro: An Advanced Semantic Chemical Editor, Visualization, and Analysis Platform. *J. Cheminform.* **2012**, *4* (1), 17. https://doi.org/10.1186/1758-2946-4-17.